



# Creating water-resistant oxygen vacancies in $\delta$ -MnO<sub>2</sub> by chlorine introduction for catalytic ozone decomposition at ambient temperature

Zhang Wu<sup>a</sup>, Pengyi Zhang<sup>a,b,\*</sup>, Shaopeng Rong<sup>c</sup>, Jingbo Jia<sup>d</sup>

<sup>a</sup> State Key Joint Laboratory of Environment Simulation and Pollution Control, School of Environment, Tsinghua University, Beijing 100084, China

<sup>b</sup> Beijing Key Laboratory for Indoor Air Quality Evaluation and Control, Beijing 100084, China

<sup>c</sup> Jiangsu Key Laboratory of Chemical Pollution Control and Resources Reuse, School of Environmental and Biological Engineering, Nanjing University of Science and Technology, Nanjing 210094, China

<sup>d</sup> State Key Laboratory of Chemical Resource Engineering, Beijing Key Laboratory of Energy Environmental Catalysis, Beijing University of Chemical Technology, Beijing 100029, China

## ARTICLE INFO

### Keywords:

Oxygen vacancies  
Mn-O bond  
Reaction intermediates  
Chlorine introduction  
DFT calculations

## ABSTRACT

To alleviate the negative impact of water vapor on ozone decomposition, we proposed a chlorine-doping strategy to create water-resistant oxygen vacancies in  $\delta$ -MnO<sub>2</sub>. Comprehensive characterizations illustrated that abundant oxygen vacancies were generated by chlorine-doping, while fewer water and intermediates accumulated during ozone decomposition. Accordingly, chlorine-doped  $\delta$ -MnO<sub>2</sub> exhibited excellent activity for ozone decomposition, keeping 97.7% removal of 2000 ppm ozone after running for 40 h under the relative humidity of 65%. DFT calculations confirmed that chlorine introduction reduced the formation energy of oxygen vacancies and enhanced the strength of Mn-O bond. The compressed Mn-O bonds liberate oxygen vacancies from being occupied by water vapor and reaction intermediates. This work demonstrates the effectiveness of chlorine introduction in creating oxygen vacancies and enhancing its resistance to water vapor, which affords a new avenue to design high-performance catalysts for ozone elimination.

## 1. Introduction

Recently atmospheric ozone pollution has become a worldwide issue [1]. Though O<sub>3</sub> absorbs short wavelength UV light in the stratosphere to protect life on earth, the ground-level O<sub>3</sub> causes ecological damage and substantial economic losses, such as reduced grain production, material degradation, and tire deterioration [2]. Long-term exposure to even low-level ozone has been associated with respiratory diseases and cardiovascular diseases [3,4]. In addition, the wide application of O<sub>3</sub> as strong oxidant in water and air purification also causes ozone pollution [5]. Therefore, it is essential to effectively eliminate O<sub>3</sub> in various situations.

The room-temperature catalytic decomposition of ozone is considered a feasible method due to its low energy consumption and non-secondary pollution emission [6–11]. A lot of catalysts such as supported noble metals (Pt [12], Pd [13], Au [14], and Ag [15,16]) and oxides transition metals of Mn [17], Fe [18], Co [19], Cu [20], and Ni [21] are widely investigated for ozone decomposition. The high cost and low

abundance of noble metals limit their wide application in most scenarios, while transition metal oxides, especially Mn-based oxides, caused much interest due to relatively high activity and low cost [22]. Oxygen vacancy (Vo) is generally regarded as the active site of transition metal oxide catalysts for ozone decomposition [23–30]. Thus, many efforts have been made to increase the content of oxygen vacancies in Mn-based catalysts, thus improving the ozone decomposition efficiency. For instance, Hong et.al [31] reported that Na<sup>+</sup> in the tunnel of  $\alpha$ -MnO<sub>2</sub> facilitated the oxygen vacancy formation. Yu et.al [32] demonstrated that moderate Cu-doping enriched oxygen vacancies in MnO<sub>2</sub>. However, the improvement to water resistance was limited owing to the hydrophilic nature of oxygen vacancies. Besides ozone, other oxygen-containing species, such as water and OH groups, may also occupy the sites of oxygen vacancies. Thus, most metal oxide catalysts face lowered activity and gradual deactivation due to the ubiquitous water vapor in air. For instance, Mn(OH)<sub>4</sub>(O<sub>2</sub>)<sup>−</sup> are regarded as adsorbed oxygen species on MnO<sub>x</sub>/Al<sub>2</sub>O<sub>3</sub>, leading to the catalyst deactivation [33]. The accumulation of intermediates like O<sub>2</sub><sup>−</sup> species on the catalyst

\* Corresponding author at: State Key Joint Laboratory of Environment Simulation and Pollution Control, School of Environment, Tsinghua University, Beijing 100084, China.

E-mail address: [zpy@tsinghua.edu.cn](mailto:zpy@tsinghua.edu.cn) (P. Zhang).

<https://doi.org/10.1016/j.apcatb.2023.122900>

Received 17 January 2023; Received in revised form 15 May 2023; Accepted 20 May 2023

Available online 22 May 2023

0926-3373/© 2023 Elsevier B.V. All rights reserved.

surface hinders the catalytic cycle of ozone decomposition[34]. In situ diffuse reflectance infrared Fourier transform spectroscopy (DRIFTS) also revealed a stable species that occurred at  $1380\text{ cm}^{-1}$  during ozone decomposition[35–39]. Thus, it is necessary to design a more effective catalyst to alleviate the accumulation of water and ozone decomposition intermediates on the sites of oxygen vacancies.

Herein, we report a strategy to create water-resistant oxygen vacancy by chlorine doping in  $\delta\text{-MnO}_2$ . The incorporation of chlorine atoms in  $\delta\text{-MnO}_2$  not only results in abundant oxygen vacancies but also makes them not easily occupied by water and ozone decomposition intermediates. Accordingly, as-synthesized chlorine-doped  $\delta\text{-MnO}_2$  achieved excellent activity in dry and humid conditions.

## 2. Experimental section

### 2.1. Catalyst preparation

A series of chlorine-doped  $\delta\text{-MnO}_2$  were synthesized by a one-pot hydrothermal process. Briefly,  $\text{KMnO}_4$  (8 mmol) and a certain amount of  $\text{NH}_4\text{Cl}$  (i.e., 4, 6, 8, 10, or 12 mmol) were dissolved in 80 mL deionized water with stirring for 30 min at room temperature. Then, the above mixture was transferred into a 100 mL Teflon-lined autoclave and maintained at  $130^\circ\text{C}$  for 30 h. After naturally cooled to the ambient temperature, the resulting precipitate was collected by filtration, then rinsed six times with deionized water, and finally dried at  $105^\circ\text{C}$  for 12 h in a vacuum oven. The as-prepared samples are denoted as  $\text{MnO}_2\text{-X}$ , in which X represents the molar ratio of  $\text{NH}_4\text{Cl}$  to  $\text{KMnO}_4$  during preparation.

### 2.2. Catalysts characterization and theoretical calculations

XRD, SEM, TEM, XPS, Raman, nitrogen adsorption, and programmed thermal desorption were used to characterize samples. In situ DRIFTS were carried out to study the ozone decomposition intermediates over  $\text{MnO}_2\text{-0.5}$  and  $\text{MnO}_2\text{-1.25}$  in dry and humid conditions. DFT calculations were employed to perform the oxygen vacancy formation energy, adsorption energy, bond strength, and reaction energy. Full details of characterization methods and DFT calculations are described in the [Supporting Information](#).

### 2.3. Evaluation of activity for ozone decomposition

The catalytic activity of as-synthesized samples was tested in a quartz tube reactor ( $\Phi = 6\text{ mm}$ ) with a certain mass of catalyst (40–60 mesh) at  $25^\circ\text{C}$ . Ozone gas (1 L/min) was generated by an ozone generator (COM-AD-01-OEM, Anshan Anseros, China). Ozone concentrations were measured with a 49i ozone analyzer (Thermo-Fisher Scientific, USA), and the inlet ozone concentration was 2000 ppm. The relative humidity (RH) was controlled by adjusting the flow rate through the water-bubbling bottle. The ozone decomposition efficiency was calculated as follows.

$$\text{Ozonere removal}(\%) = \frac{[\text{O}_3]_{\text{in}} - [\text{O}_3]_{\text{out}}}{[\text{O}_3]_{\text{in}}} \times 100\% \quad (1)$$

where  $[\text{O}_3]_{\text{in}}$  and  $[\text{O}_3]_{\text{out}}$  are the ozone concentrations in the inlet and outlet gas, respectively.

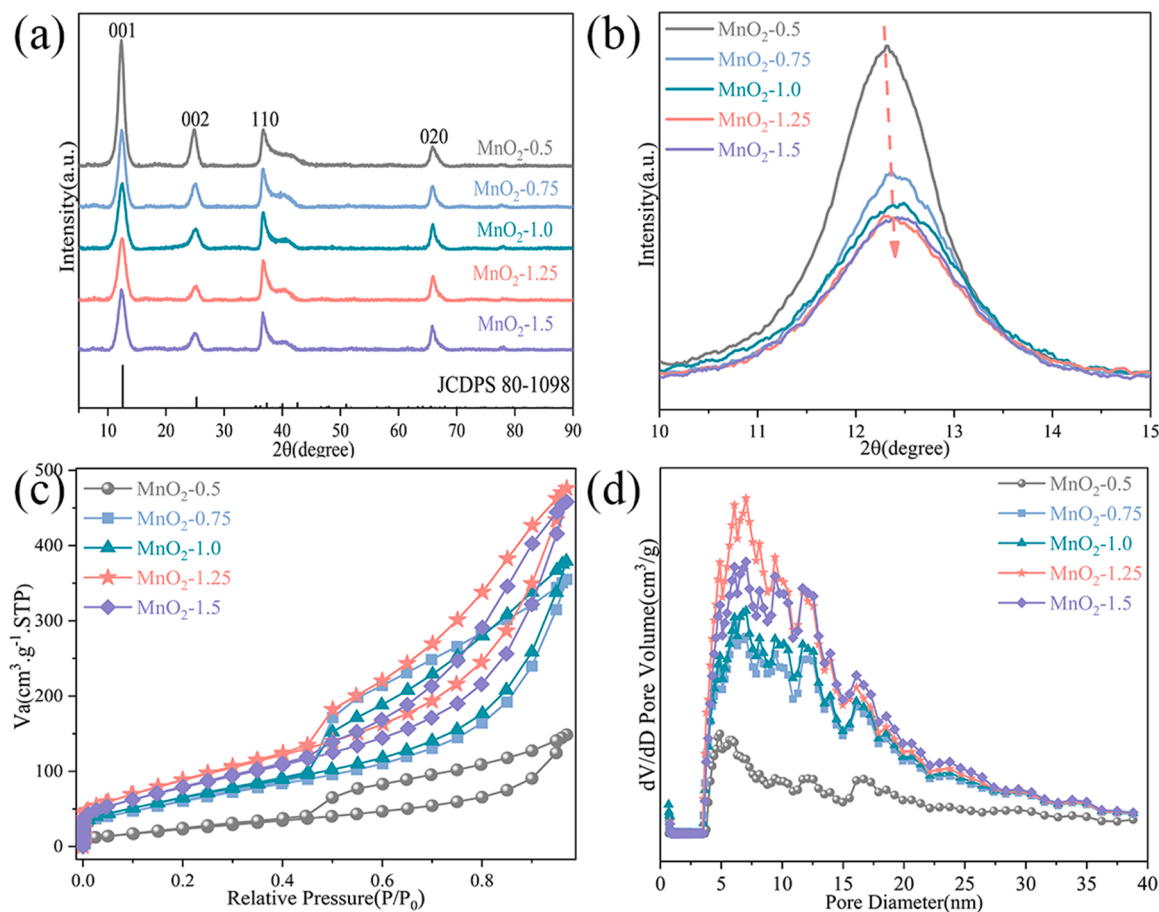


**Fig. 1.** (a) XRD patterns; (b) The enlarged view of the  $\delta\text{-MnO}_2$  (001) peak. (c)  $\text{N}_2$  adsorption-desorption isotherms; (d) The pore size distributions analyzed by using nonlocal density functional theory (NLDF, DFT kernel:  $\text{N}_2$  at 77 K on silica-based on a cylindrical/sphere pore model using the adsorption branch).

### 3. Results and discussion

#### 3.1. Crystal and textural properties of catalysts

XRD was used to check the impact of chlorine doping on the crystallinity of samples. As shown in Fig. 1a, the diffraction peaks of all samples matched well with  $\delta$ -MnO<sub>2</sub> (JCPDS No.80–1098)[40]. With the increase of chlorine doping, the diffraction peak assigned to the (001) facets decreased, implying the more distorted structure and defects. The distortion can be ascribed to the different radius between doped Cl (180 pm) and replaced O (140 pm). The lattice distortion is severe, and crystal defects such as oxygen vacancies are more likely to occur[41]. The increased chlorine doping also makes the (001) peak slightly shift to larger diffraction angles (Fig. 1b), indicating the interlayer spacing is slightly reduced.

The N<sub>2</sub> adsorption-desorption isotherms of as-synthesized catalysts are shown in Fig. 1c. All samples present type IV isotherms with H2 hysteresis loop at  $P/P_0 = 0.5$ – $0.9$ , suggesting the presence of a mesoporous structure. Fig. 1d shows the pore size distribution. As summarized in Table 1, the average pore size increased with the increase of Cl content, as well as the specific surface area. As capillary water condensation is more difficult to occur in larger pores[42], the above result implies that chlorine doping can retard the condensation of water vapor and accordingly increase the water resistance.

The surface morphology was checked with SEM and TEM. As shown in Fig. 2, all samples look like microspheres. The MnO<sub>2</sub>-0.5 and MnO<sub>2</sub>-0.75 samples mainly consisted of 3–4  $\mu$ m microspheres, while MnO<sub>2</sub>-1.0, MnO<sub>2</sub>-1.25, and MnO<sub>2</sub>-1.5 mainly consisted of < 1  $\mu$ m microspheres. TEM images further reveal that these microspheres were assembled with nanosheets. Furthermore, HRTEM images (Fig. 2i and 2k) show lattice fringes of  $\sim 0.7$  nm and 0.248 nm corresponding to the interplanar distance of (001) and (110) facets of  $\delta$ -MnO<sub>2</sub>, respectively [43,44]. However, MnO<sub>2</sub>-0.5 shows regular and smooth lattice stripes, whereas obscure lattice fringes can be observed in MnO<sub>2</sub>-1.25, which is consistent with the XRD results. In addition, EDX-mappings (Fig. S1) show that the Cl element is evenly distributed in the MnO<sub>2</sub>-0.5 and MnO<sub>2</sub>-1.25, which confirmed the presence of chlorine in the chlorine-doped MnO<sub>2</sub>.

#### 3.2. Surface chemical components and active oxygen species

XPS survey (Fig. 3a) shows that all chlorine-doped MnO<sub>2</sub> samples consisted of the elements Mn, K, Cl, and O, and there was no N1s characteristic peak in the survey spectrum. In the Cl 2p spectra (Fig. 3b), the peaks at 198.4 eV and 200 eV corresponded to Cl 2p<sub>1/2</sub> and Cl 2p<sub>3/2</sub> [45,46], respectively, confirming that Cl was successfully incorporated into  $\delta$ -MnO<sub>2</sub>. And the Cl peaks obviously increased with the order of MnO<sub>2</sub>-0.5 < MnO<sub>2</sub>-0.75 < MnO<sub>2</sub>-1.0 < MnO<sub>2</sub>-1.25 < MnO<sub>2</sub>-1.5, which is consistent with the bulk Cl content determined by ion chromatography (Table 2). The average oxidation state (AOS) of Mn was calculated according to the Mn 3s splitting energy  $\Delta E$ , i.e.,  $AOS = 8.956 - 1.123 * \Delta E$  (Fig. 3c). As listed in Table 2, the AOS of Mn decreased with the increasing content of Cl, indicating the Cl-doping increase the amount of Mn<sup>3+</sup> in  $\delta$ -MnO<sub>2</sub>. The O1s spectra (Fig. 3d) can be deconvoluted into three peaks at 529.9, 531.6, and 533.0 eV, corresponding to the lattice oxygen (O<sup>2-</sup>), surface adsorbed oxygen species

(O<sub>ads</sub>), and surface adsorbed water (H<sub>2</sub>O), respectively[35,36]. As summarized in Table 2, MnO<sub>2</sub>-1.25 has the highest ratio of O<sub>ads</sub>.

Surface-adsorbed oxygen species are generally related to oxygen vacancies and catalytic oxidation activity[47,48]. Thus, we further used H<sub>2</sub>-TPR and O<sub>2</sub>-TPD to check the reducibility of these surface-adsorbed oxygen species. As shown in Fig. 4a, only one broad peak occurred in the H<sub>2</sub>-TPR profiles. As seen in the inset of Fig. 4a, the onset peak increased with the increasing Cl content except for the MnO<sub>2</sub>-1.5 sample. Furthermore, the H<sub>2</sub> consumption summarized in Fig.S2 also was in the order of MnO<sub>2</sub>-0.5 < MnO<sub>2</sub>-0.75 < MnO<sub>2</sub>-1.0 < MnO<sub>2</sub>-1.5 < MnO<sub>2</sub>-1.25, indicating that MnO<sub>2</sub>-1.25 contained the most active oxygen species.

The O<sub>2</sub>-TPD (Fig. 4b) signals can be divided into three regions: surface active oxygen species (<300 °C), sub-surface lattice oxygen (300 °C –600 °C) and bulk lattice oxygen (>600 °C). MnO<sub>2</sub>-1.25 showed the largest amount of labile oxygen among all samples, which is in good agreement with XPS O1s spectra and H<sub>2</sub>-TPR profiles.

The above results of XPS, H<sub>2</sub>-TPR, and O<sub>2</sub>-TPD indicate that chlorine-doping significantly induces abundant surface oxygen species, which is closely related to oxygen vacancies. To confirm the presence of oxygen vacancies and compare their contents in these samples, ESR analysis was conducted (Fig. 4c). All samples showed a symmetric signal with a g-value of 2.004, which can be attributed to the electrons trapped in the oxygen vacancies. Moreover, the signal intensity almost increased with the increase of Cl content. The MnO<sub>2</sub>-1.25 sample exhibited the highest signal intensity, though the signal of MnO<sub>2</sub>-1.5 slightly decreased due to excessive chlorine doping. These results further confirmed that MnO<sub>2</sub>-1.25 possessed more oxygen vacancies than other samples.

To further reveal the surface structures of MnO<sub>2</sub>-X, the samples were characterized by Raman spectra (Fig. 4d). Raman spectra exhibited a series of distinct bands[49,50]. The main band at around 500 cm<sup>-1</sup> could be assigned to the stretching vibration of Mn-O-Mn. The peak at 569 cm<sup>-1</sup> was attributed to the stretching vibration of  $\nu_3$  (Mn-O), which is usually regarded as a tool to predict the amount of Mn<sup>4+</sup>[51]. With the increase of Cl content, the signal at 569 cm<sup>-1</sup> gradually weakened, indicating the gradual decrease of Mn<sup>4+</sup> content. The peak at 640 cm<sup>-1</sup> corresponding to the vibration of  $\nu_2$  (Mn-O) remarkably decreased with the increased Cl doping. The bond force constant (k) representing the Mn-O bond strength can be estimated according to Hooke's law[50]. The higher frequency of  $\nu_2$  (Mn-O) indicates the larger force constant and stronger Mn-O bond. Therefore, this result demonstrates that chlorine doping not only induces more oxygen vacancies but also makes the Mn-O bond stronger. The stronger Mn-O bond implies the weak interaction of Mn with the nearby oxygen vacancy site, thus the oxygen vacancy become more stable to alleviate the occupation by water molecules.

#### 3.3. Ozone decomposition performance

The performance of as-synthesized chlorine-doping  $\delta$ -MnO<sub>2</sub> for 2000 ppm ozone decomposition at 25 °C is shown in Fig. 5. Under dry condition (3.1 ppm H<sub>2</sub>O) and the weight hourly space velocity (WHSV) of 1200 L/g<sub>cat</sub>.h, only the MnO<sub>2</sub>-1.25 sample exhibited excellent and stable performance within 180 min. Other samples significantly decreased their efficiency. For example, the MnO<sub>2</sub>-0.5 sample decreased from initial 93.8–61.6% (Fig. 5a), which can be ascribed to the loss of

**Table 1**  
Specific surface area and pore analysis results.

Samples	BET (m <sup>2</sup> /g)	Pore diameter (nm)	Pore volume (cm <sup>3</sup> /g)	H <sub>2</sub> consumption (mmol.g <sup>-1</sup> )	Henry's law constant
MnO <sub>2</sub> -0.5	84	4.89	0.23	9.184	1.62
MnO <sub>2</sub> -0.75	208	6.08	0.55	9.219	0.50
MnO <sub>2</sub> -1.0	225	7.03	0.59	9.761	0.34
MnO <sub>2</sub> -1.25	312	7.03	0.74	9.881	0.29
MnO <sub>2</sub> -1.5	278	7.03	0.71	9.880	0.22



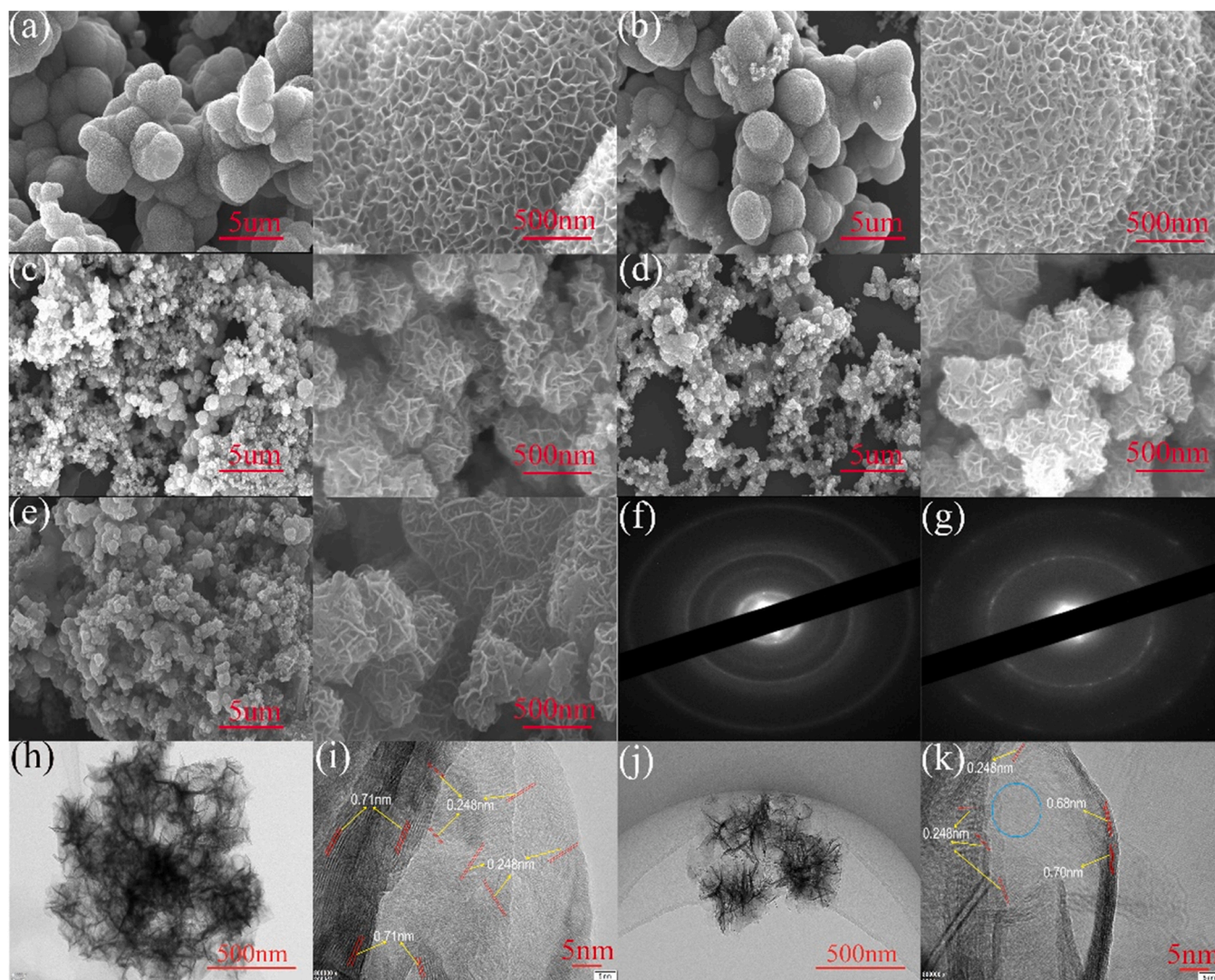


Fig. 2. FESEM images of (a)  $\text{MnO}_2\text{-0.5}$ , (b)  $\text{MnO}_2\text{-0.75}$ , (c)  $\text{MnO}_2\text{-1.0}$ , (d)  $\text{MnO}_2\text{-1.25}$ , and (e)  $\text{MnO}_2\text{-1.5}$ ; SAED images of (f)  $\text{MnO}_2\text{-0.5}$  and (g)  $\text{MnO}_2\text{-1.25}$ ; TEM images and HRTEM images of (h, i)  $\text{MnO}_2\text{-0.5}$  and (j, k)  $\text{MnO}_2\text{-1.25}$ .

some oxygen vacancies[40]. When the WHSV decreased to 600 L/g.h and RH increased to 65%,  $\text{MnO}_2\text{-1.25}$  still maintained  $\sim 100\%$  removal of ozone after 180 min continuous running (Fig. 5b). Though under this condition other samples still clearly decreased their activity with test time to a varying degree, the decreasing trend became slowly, indicating the effect of operation conditions on the catalyst performance. The above results demonstrate that chlorine-doped  $\text{MnO}_2\text{-1.25}$  exhibited the best activity among all samples. The superiority of  $\text{MnO}_2\text{-1.25}$  for ozone decomposition can be attributed to the reducibility, compact particle sizes, high specific area and abundant oxygen vacancies as illustrated in Sections 3.1 and 3.2.

The performances of  $\text{MnO}_2\text{-1.25}$  under other relative humidity under the WHSV of 600 L/g.h are shown in Fig. 5c. The activities of  $\text{MnO}_2\text{-1.25}$  under RH 35% and RH 65% are very close to that under dry condition (3.1 ppm  $\text{H}_2\text{O}$ ). When the RH increased to 90%, the activity decreased obviously, which can be ascribed to the enhanced water competitive adsorption due to the capillary condensation effect under high humidity. However, after a period of time, the ozone removal efficiency over  $\text{MnO}_2\text{-1.25}$  reached a relatively stable state, indicating that a high portion of oxygen vacancies can still act as active sites for ozone decomposition even under high humidity. As we know, the water concentration of RH 65% and 90% at 25 °C is as high as 20,332 ppm and 28,152 ppm, respectively, which is 10 times higher than the ozone

concentration (2000 ppm) adopted in the test. The above result indicates it is not easy for water vapor to compete with ozone to occupy sites of oxygen vacancies.

The performance of  $\text{MnO}_2\text{-1.25}$  under alternate RH 90% and RH 65% under the WHSV of 600 L/g.h was also tested, as well as of  $\text{MnO}_2\text{-0.5}$  for comparison (Fig. 5d). Though the ozone removal efficiency over  $\text{MnO}_2\text{-1.25}$  under RH 90% decreased a lot, it soon recovered to nearly 100% when the RH switched to 65%. Moreover, after 14 h alternate running, it almost kept its original activity. However,  $\text{MnO}_2\text{-0.5}$  exhibited apparent activity attenuation. Furthermore, the long-time performance of  $\text{MnO}_2\text{-1.25}$  under RH 65% and the WHSV of 600 L/g.h was tested (Fig. 5e).  $\text{MnO}_2\text{-1.25}$  kept stable and high ozone removal efficiency (97.7%) in the 40-h test. The above results clearly demonstrate the excellent activity and stability of  $\text{MnO}_2\text{-1.25}$  for ozone decomposition under various humid conditions. The enhanced stability and improved water-resistance originated from the stronger Mn-O bond by Cl introduction, which will be further illustrated by DFT calculations below. In comparison with other Mn-based catalysts reported in the literature (Table. S1),  $\text{MnO}_2\text{-1.25}$  in this study showed the best activity for ozone decomposition.



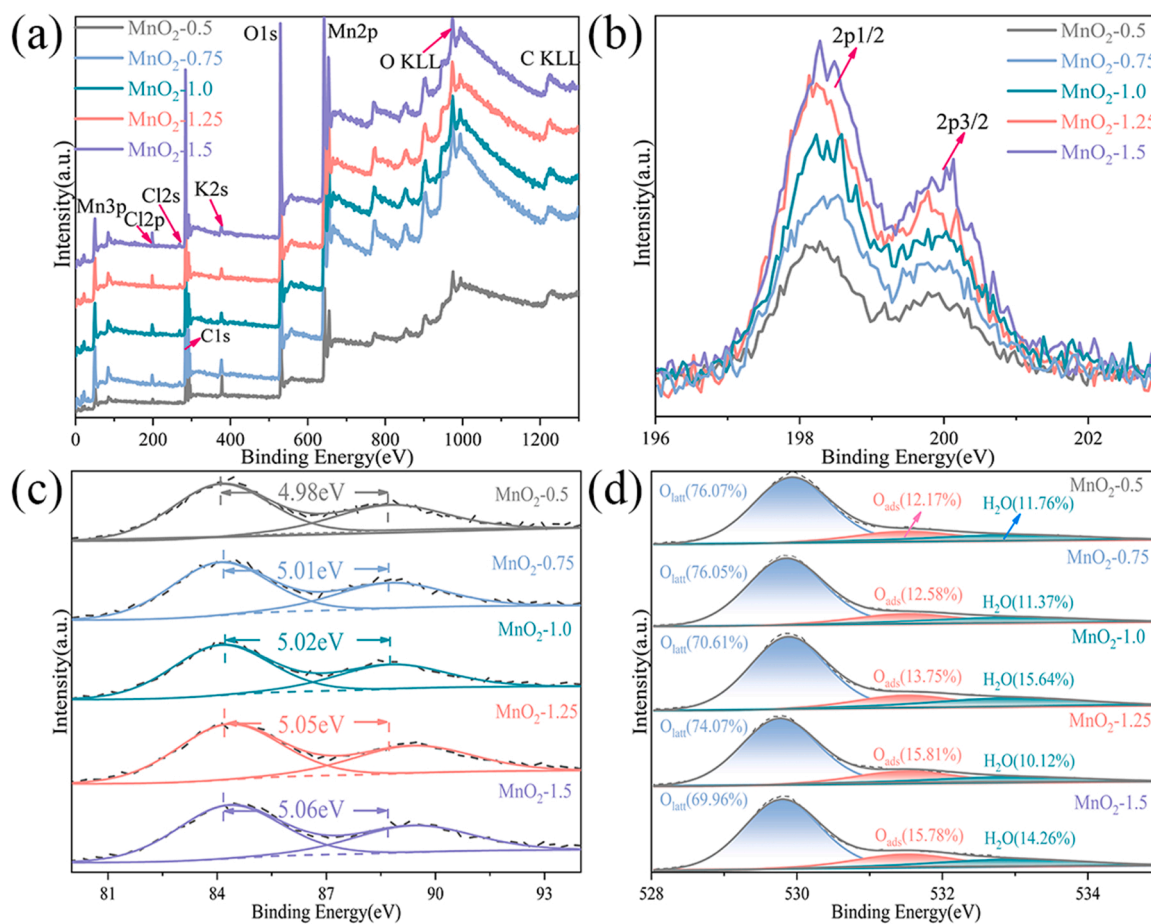


Fig. 3. XPS spectra of the as-synthesized catalysts. (a) Survey, (b) Cl 2p, (c) Mn 3 s, and (d) O 1 s.

Table 2

Elemental compositions of chlorine-doped MnO<sub>2</sub> samples.

Samples	Molar ratio by XPS		Mn AOS	O1s by XPS (%)			ICP K/Mn	IC Cl (%)
	Cl/Mn	K/Mn		O <sub>latt</sub>	O <sub>ads</sub>	H <sub>2</sub> O		
MnO <sub>2</sub> -0.5	0.018	0.29	3.35	76.07	12.17	11.76	0.132	0.06
MnO <sub>2</sub> -0.75	0.034	0.20	3.31	76.05	12.58	11.37	0.109	0.48
MnO <sub>2</sub> -1.0	0.039	0.19	3.30	70.61	13.75	15.64	0.103	1.00
MnO <sub>2</sub> -1.25	0.065	0.17	3.27	74.07	15.81	10.12	0.102	1.60
MnO <sub>2</sub> -1.5	0.067	0.14	3.26	69.96	15.78	14.26	0.089	2.20

### 3.4. Ozone decomposition pathways revealed by in situ DRIFTS

To deeply understand why MnO<sub>2</sub>-1.25 had excellent performance, we used in situ DRIFTS to detect the surface species of MnO<sub>2</sub>-1.25 under various conditions, as well as MnO<sub>2</sub>-0.5 for comparison. It is well known that oxygen vacancies may be competitively occupied by water molecules besides ozone [52,53]. However, Raman spectra analysis indicated that MnO<sub>2</sub>-1.25 had a stronger Mn-O bond, implying that MnO<sub>2</sub>-1.25 was not easily surface-hydroxylated and more resistant to water vapor. To verify it, in situ DRIFTS of MnO<sub>2</sub>-0.5 and MnO<sub>2</sub>-1.25 under the H<sub>2</sub>O/N<sub>2</sub> flow were checked. As shown in Figs. 6a and 6b, strong peaks occurred at 1650 cm<sup>-1</sup>, and ~3000–3600 cm<sup>-1</sup>, which can be ascribed to the shear vibration of surface adsorbed water and the stretching mode of water or surface hydroxyl groups, respectively [54]. The broad peaks at 700–950 cm<sup>-1</sup> and 1200–1500 cm<sup>-1</sup> can be ascribed to some surface oxygen species due to the dissociation of water [55,56]. The intensities of these peaks on MnO<sub>2</sub>-1.25 were much weaker than those on MnO<sub>2</sub>-0.5, indicating less water adsorption and subsequent dissociation on MnO<sub>2</sub>-1.25. As mentioned above, MnO<sub>2</sub>-1.25 had a much higher

content of oxygen vacancies than MnO<sub>2</sub>-0.5. Thus, the present result indicates that the chlorine-doping induced oxygen vacancies in MnO<sub>2</sub>-1.25 are not easily occupied by water vapor or OH groups, i.e., more resistant to water vapor. To further verify the effect of Cl on water adsorption, the water vapor isotherms for the as-prepared catalysts were investigated (as shown in Fig. S3). The Henry's law constant was calculated according to the virial model [57,58]. As clearly shown in Table 1, the lower Henry's law constant indicates that the more chlorine addition significantly decreased the H<sub>2</sub>O adsorption on the surface of catalysts.

Next, the in-situ DRIFTS under the dry O<sub>3</sub> condition were investigated. As shown in Fig. 6c of MnO<sub>2</sub>-0.5, two small peaks at 1025 cm<sup>-1</sup> and 1050 cm<sup>-1</sup> attributed to the surface adsorbed O<sub>3</sub> [59] occurred and gradually increased with test time, indicating that O<sub>3</sub> adsorbed on the surface of MnO<sub>2</sub>-0.5. In addition, the intensity of surface hydroxyl groups (3650 cm<sup>-1</sup>) decreased with time, while simultaneously a tiny peak at 1610 cm<sup>-1</sup> was assigned to water and a strong peak at 1370 cm<sup>-1</sup> occurred. As mentioned above, water vapor was more easily adsorbed and dissociated into surface OH groups on MnO<sub>2</sub>-0.5 than on

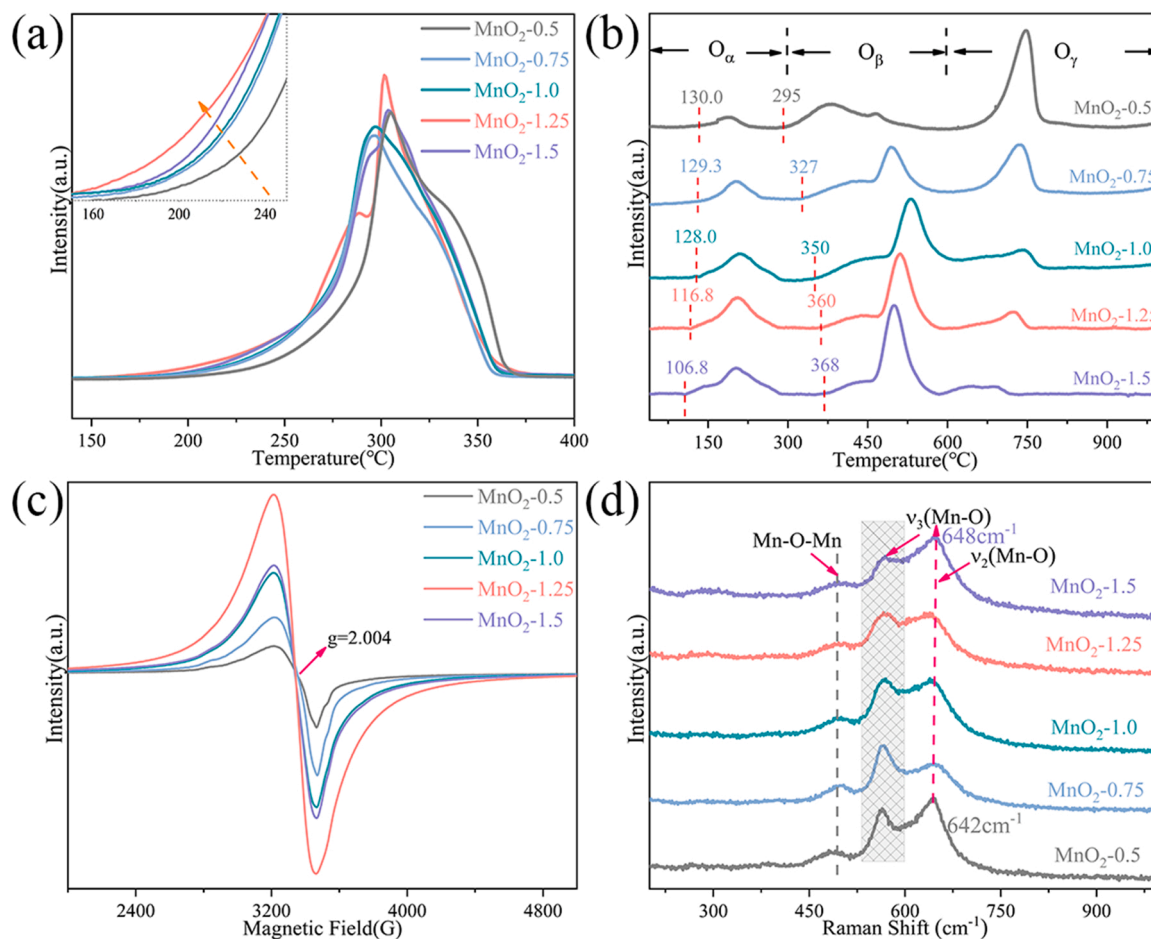


Fig. 4. (a)  $\text{H}_2$ -TPR, (b)  $\text{O}_2$ -TPD, (c) ESR and (d) Raman spectra of as-synthesized catalysts.

$\text{MnO}_2$ -1.25 (Figs. 6a and 6b). Thus, the present results indicate that surface OH groups on  $\text{MnO}_2$ -0.5 may react with ozone and are converted into adsorbed water occurring at  $1610\text{ cm}^{-1}$  and relatively stable oxygen species occurring at  $1370\text{ cm}^{-1}$ , which can be assigned to surface  $\text{HO}_2$  specie according to the calculation of density-functional perturbation theory [60]. As for the  $\text{MnO}_2$ -1.25 (Fig. 6d), there was no signal at  $1370\text{ cm}^{-1}$ , and a small peak at  $1110\text{ cm}^{-1}$  corresponding to the superoxide species ( $\text{O}_2^-$ ) [61] occurred, while in the case of  $\text{MnO}_2$ -0.5 peroxide species ( $\text{O}_2^{2-}$ ) ( $820\text{--}980\text{ cm}^{-1}$ ) [62,63] rather than superoxide species occurred. Both superoxide and peroxide species are possible intermediates when ozone decomposes via the oxygen-vacancy mechanism. As mentioned above,  $\text{MnO}_2$ -1.25 has stronger Mn-O bonds than  $\text{MnO}_2$ -0.5. Thus, it is reasonable that Mn atoms of  $\text{MnO}_2$ -1.25 could provide fewer electrons to  $\text{O}_3$  and accordingly  $\text{O}_2^-$  preferentially formed during ozone decomposition in the case of  $\text{MnO}_2$ -1.25.

The in-situ DRIFTS were further investigated under the humid  $\text{O}_3$  condition. As for  $\text{MnO}_2$ -0.5 (Fig. 6e), strong peaks at  $1650\text{ cm}^{-1}$  and  $\sim 3000\text{--}3600\text{ cm}^{-1}$  corresponding to water and hydroxyl groups occurred, which was similar to the phenomena under the  $\text{H}_2\text{O}/\text{N}_2$  flow (Fig. 6a). However, only a tiny peak occurred at  $1370\text{ cm}^{-1}$ , which was much different from that under the dry  $\text{O}_3$  condition (Fig. 6c). The inhibited accumulation of the  $1370\text{ cm}^{-1}$  peak by water vapor was also found on the alumina surface [64]. As mentioned above, the  $1370\text{ cm}^{-1}$  peak can be regarded as the reaction product ( $\text{HO}_2$ ) of  $\text{O}_3$  with surface OH groups. Thus the present result implies that water vapor is more competitive than ozone in combining with surface OH groups of  $\text{MnO}_2$ -0.5. Thus the formation of  $1370\text{ cm}^{-1}$  peak was inhibited. In addition, stronger peaks assigned to adsorbed ozone, peroxide species, and ozonide ion ( $\text{O}_3^-$ ) at  $\sim 800\text{ cm}^{-1}$  (Table S2 and S3) occurred, which

indicated ozone decomposition and desorption of intermediates from  $\text{MnO}_2$ -0.5 became slower under the humid condition than under the dry condition. Much weaker DRIFTS peaks were observed on  $\text{MnO}_2$ -1.25 (Fig. 6f) than on  $\text{MnO}_2$ -0.5, indicating less adsorption of water and faster desorption of ozone decomposition intermediates from  $\text{MnO}_2$ -1.25, i.e., the ozone decomposition on  $\text{MnO}_2$ -1.25 was less influenced by water vapor. In addition, it is worth noting that the peak at  $\sim 3000\text{--}3600\text{ cm}^{-1}$  (contributed by  $\text{H}_2\text{O}$  and surface OH group) under the humid  $\text{O}_3$  condition was much smaller than under the  $\text{H}_2\text{O}/\text{N}_2$  condition, implying adsorbed water and surface hydroxyl groups may participate in the ozone decomposition reaction.

The above in-situ DRIFTS analysis clearly confirms that chlorine-doping not only generates abundant oxygen vacancies but also efficiently enhances their resistance to water vapor. Accordingly, the  $\text{MnO}_2$ -1.25 catalyst showed excellent activity in decomposing ozone under dry and humid conditions.

According to the intermediates identified by in situ DRIFTS and oxygen vacancy-based mechanisms, the ozone decomposition pathways on chlorine-doped  $\text{MnO}_2$  are proposed as follows. Under the dry condition, ozone decomposes via the following steps (D1-D5), in which both peroxide and superoxide species are included as ozone decomposition intermediates, while only the peroxide species intermediate is reported in the literature [65].



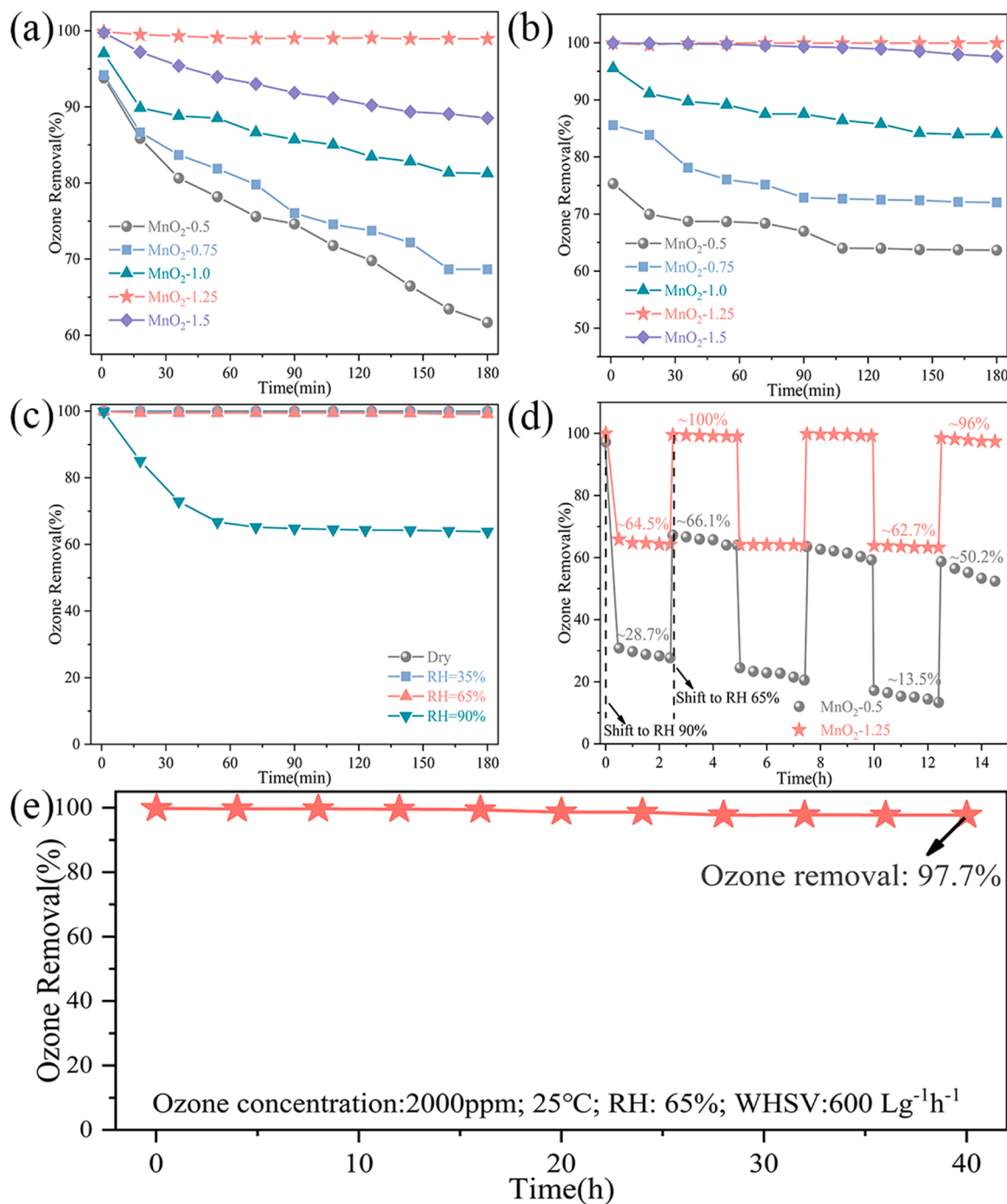
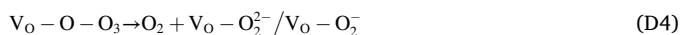
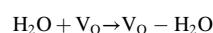


**Fig. 5.** Performance of chlorine-doped  $\delta$ -MnO<sub>2</sub> for 2000 ppm ozone at 25 °C under different conditions. (a) under dry condition (3.1 ppm H<sub>2</sub>O); (b) under RH 65%; (c) performance of MnO<sub>2</sub>-1.25 under different RH; (d) performance of MnO<sub>2</sub>-1.25 and MnO<sub>2</sub>-0.5 under alternate RH 90% and RH 65%; (e) long-time performance of MnO<sub>2</sub>-1.25 under RH 65%. The WHSV in (a) was 1200 L/g<sub>cat</sub>·h, while in (b), (c), (d) and (e) it was 600 L/g<sub>cat</sub>·h.



Under the humid condition, besides the pathways mentioned above, water may also participate in the catalytic cycle (Fig. 7). First, water molecules may be adsorbed to the oxygen vacancy sites, forming adsorbed H<sub>2</sub>O (step H1 in the case of MnO<sub>2</sub>-1.25) and surface OH groups (step H2-1a in the case of MnO<sub>2</sub>-0.5). Then, ozone reacts with the surface hydroxyl group (H2-1b in the case of MnO<sub>2</sub>-0.5) or adsorbed water (H2-2 in the case of MnO<sub>2</sub>-1.25). After subsequent reaction steps (H3-

H8), ozone is finally decomposed, and oxygen vacancy is recovered. Intermediates involved in this cycle, such as adsorbed HO<sub>2</sub>, superoxide, and peroxide species were confirmed by in-situ DRIFTS. The ozonic acid (HO<sub>3</sub>) was reported as intermediate for ozone decomposition in the literatures[36,66]. It is reasonable that ozone as a weak base reacts with hydroxyl groups (Bronsted acid) or H<sub>2</sub>O to form HO<sub>3</sub>. Furthermore, many researchers reported that the HO<sub>3</sub> as a sort of free radical species easily decomposed into hydroxyl radicals and superoxide species[67]. In addition, all intermediate reactions were confirmed by DFT calculations, which were presented in Fig. S8.





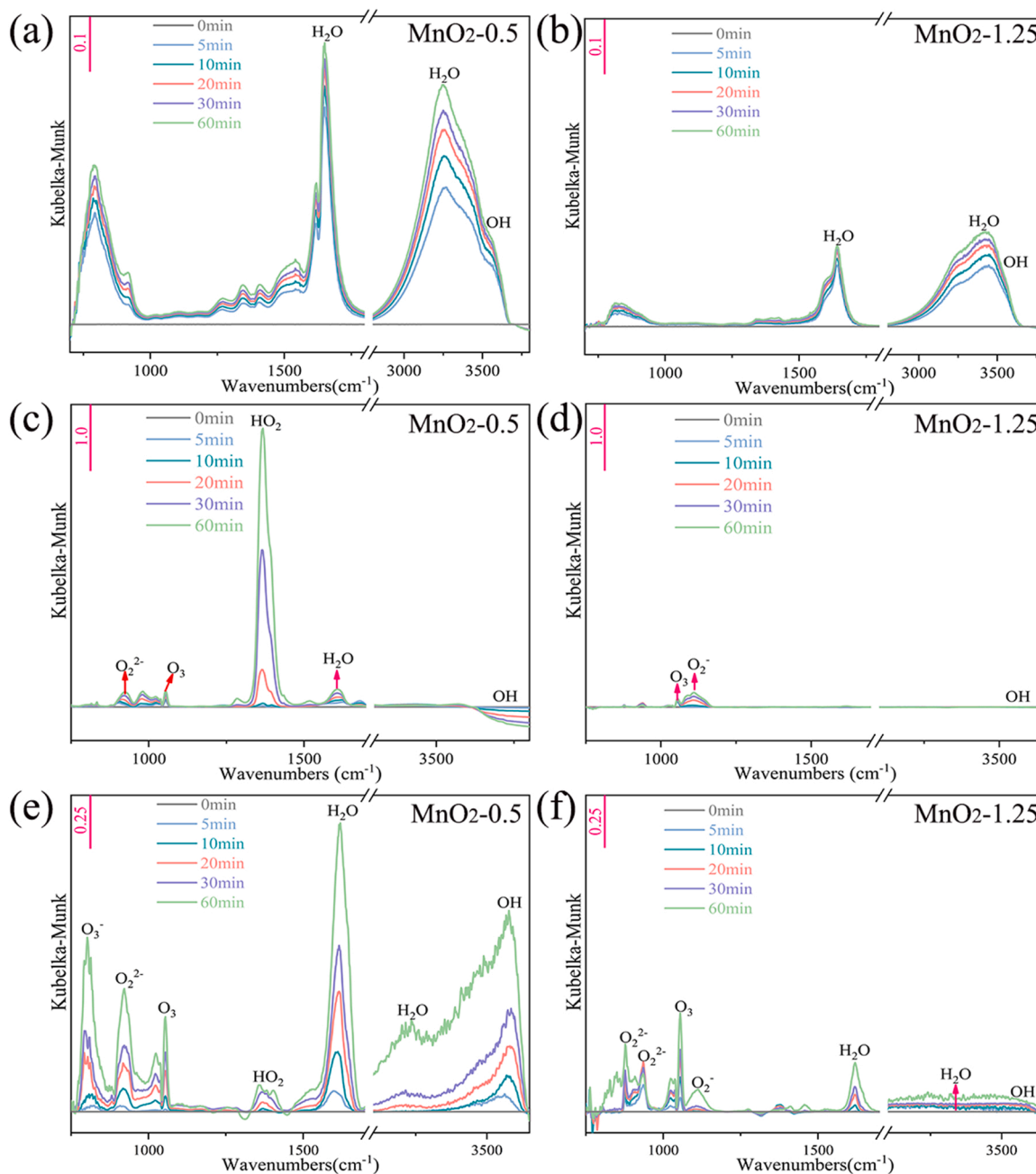
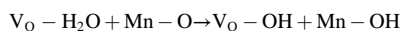
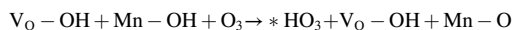


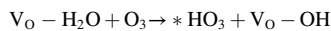
**Fig. 6.** In situ DRIFTS of MnO<sub>2</sub>-0.5 and MnO<sub>2</sub>-1.25 under various conditions. (a, b) under the H<sub>2</sub>O/N<sub>2</sub> flow; (c, d) under the dry O<sub>3</sub>/O<sub>2</sub> flow; (e, f) under the humid O<sub>3</sub>/O<sub>2</sub> flow.



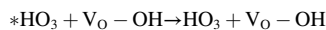
H2-1a



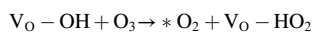
H2-1b



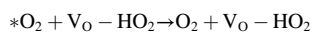
H2-2



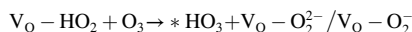
H3



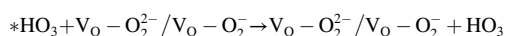
H4



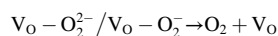
H5



H6



H7



H8

### 3.5. The role of chlorine doping illustrated by DFT calculations

To essentially understand why chlorine introduction was beneficial to generate water-resistant oxygen vacancies in  $\delta$ -MnO<sub>2</sub> for ozone decomposition, DFT calculations were further performed. First, we established models of  $\delta$ -MnO<sub>2</sub> with various concentrations of Cl (Fig. S4) to investigate the effect of chlorine doping on surface oxygen vacancy formation. The calculation results in Fig. 8a indicate that with the increase of Cl content, the formation energy of oxygen vacancy in  $\delta$ -MnO<sub>2</sub> surfaces decreases, demonstrating that the presence of Cl atom is beneficial to the formation of nearby oxygen vacancies.

Next, we calculated the bond strength of Mn-O on the surface, which is closely related to the reactivity of Mn atom and stability of the nearby

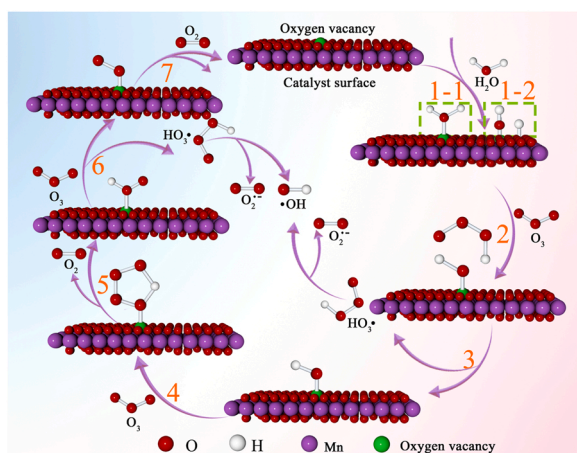


Fig. 7. Proposed ozone decomposition pathway under humid condition. Stage 1–1 represents non-dissociative adsorption of  $\text{H}_2\text{O}$ , 1–2 represents dissociative adsorption of  $\text{H}_2\text{O}$ .

oxygen vacancies[51]. As shown in Fig. 8b, the calculated strength of Mn–O bonds in the vacancy-free  $\text{MnO}_2$  is 340.49 KJ/mol, decreasing to 338.50 KJ/mol in the oxygen-vacant  $\text{MnO}_2$  ( $\text{MnO}_2\text{-Vo}$ ). This result indicates that the presence of oxygen vacancy weakens the adjacent Mn–O bonds by stretching them. Accordingly, the binding potential of Mn with the nearby oxygen vacancy becomes strong, i.e., the oxygen vacancy can be more easily occupied by reactants such as water. However, the chlorine-doping obviously increased the bond strength of Mn–O, which is calculated as 345.8 KJ/mol in the chlorine-doped  $\text{MnO}_2$  model ( $\text{MnO}_2\text{-Cl}$ ). Moreover, the bond strength of Mn–O further increases with the increasing content of oxygen vacancies in  $\text{MnO}_2\text{-Cl}$ . The strengthened Mn–O bond becomes more challenging to be broken. Accordingly, the binding potential of Mn with nearby oxygen vacancy becomes weak, i.e., the reactivity of oxygen vacancy decreases to some extent.

To verify the above calculation results, we further calculated the adsorption energy of  $\text{O}_3$ ,  $\text{O}_2$ , and  $\text{H}_2\text{O}$  on the  $\text{MnO}_2$  surface. As shown in Fig. 9,  $\text{O}_3$ ,  $\text{O}_2$ , and  $\text{H}_2\text{O}$  prefer to adsorb on the oxygen vacancy sites of the non-chlorine-doped  $\text{MnO}_2$  slab ( $\text{MnO}_2\text{-Vo}$ ). However, the adsorption energies of  $\text{H}_2\text{O}$ ,  $\text{O}_2$ , and  $\text{O}_3$  on the oxygen vacancy site of chlorine-doped  $\text{MnO}_2$  ( $\text{MnO}_2\text{-Cl-Vo}$ ) are obviously weaker than those on  $\text{MnO}_2\text{-Vo}$ , which confirms the result from the bond strength analysis, i.e., the chlorine-doping decreases the reactivity of oxygen vacancy to some extent. Interestingly, though both adsorption energies of  $\text{H}_2\text{O}$  and  $\text{O}_3$  on  $\text{MnO}_2\text{-Cl-Vo}$  are correspondingly weaker than those on  $\text{MnO}_2\text{-Vo}$ , the adsorption energy of  $\text{H}_2\text{O}$  was decreased much more than that of  $\text{O}_3$ . As

a result,  $\text{O}_3$  exhibits more advantages over  $\text{H}_2\text{O}$  on adsorption on  $\text{MnO}_2\text{-Cl-Vo}$ , i.e., the chlorine-doping enhances the resistance of oxygen vacancy to water vapor. Fig. 9.

Finally, we calculated the reaction energy of each elementary reaction during ozone decomposition over  $\text{MnO}_2\text{-Vo}$  like  $\text{MnO}_2\text{-0.5}$  and  $\text{MnO}_2\text{-Cl-Vo}$  like  $\text{MnO}_2\text{-1.25}$ . First, the calculation was performed for the dry  $\text{O}_3$  decomposition pathway, i.e., steps D1–D5. The clean (001) plane with a Vo site was taken as the reference. The atomic structure in each step is presented in Fig. S5. As shown in Fig. 10a, the elementary reaction D3 and D5 are endothermic, thus they may become the rate-limiting steps. D3 reaction represents the adsorption of the second  $\text{O}_3$  molecule with the active oxygen atom on the Vo site, while the D5 reaction shows the desorption of dioxygen species ( $\text{O}_2^*$  or  $\text{O}_2$ ) from the Vo site. The free energy barriers of D3 for two different slabs are very close, while the desorption energy of dioxygen species from  $\text{MnO}_2\text{-Cl-Vo}$  (0.03 eV) in D5 is significantly smaller than that from  $\text{MnO}_2\text{-Vo}$  (0.174 eV), which validates that the chlorine-doping significantly increases the ozone decomposition efficiency under dry condition.

The structure models of ozone decomposition over  $\text{MnO}_2\text{-Vo}$  and  $\text{MnO}_2\text{-Cl-Vo}$  under humid condition are shown in Fig. S6 and Fig. S7, respectively. The reaction energy of each elementary reaction is shown in Fig. 10b. Over the  $\text{MnO}_2\text{-Vo}$  slab, the first step (H1) is the adsorption of  $\text{H}_2\text{O}$  on oxygen vacancy. It is an exothermic process with  $\Delta G$  of  $-0.65$  eV, which is sufficient to overcome the reaction barrier to the transition state (from  $-0.65$  eV to  $-0.13$  eV). Thus, dissociative and

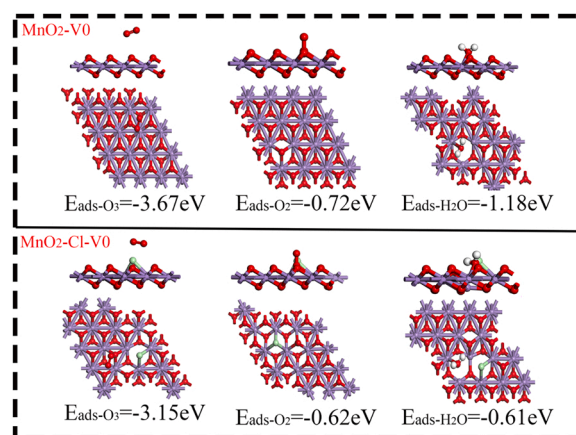


Fig. 9. The calculated adsorption energies of  $\text{O}_3$ ,  $\text{O}_2$  and  $\text{H}_2\text{O}$  on  $\text{MnO}_2\text{-Vo}$  and  $\text{MnO}_2\text{-Cl-Vo}$  (purple, red, green, and white balls represent Mn, O, Cl, and H atoms, respectively).

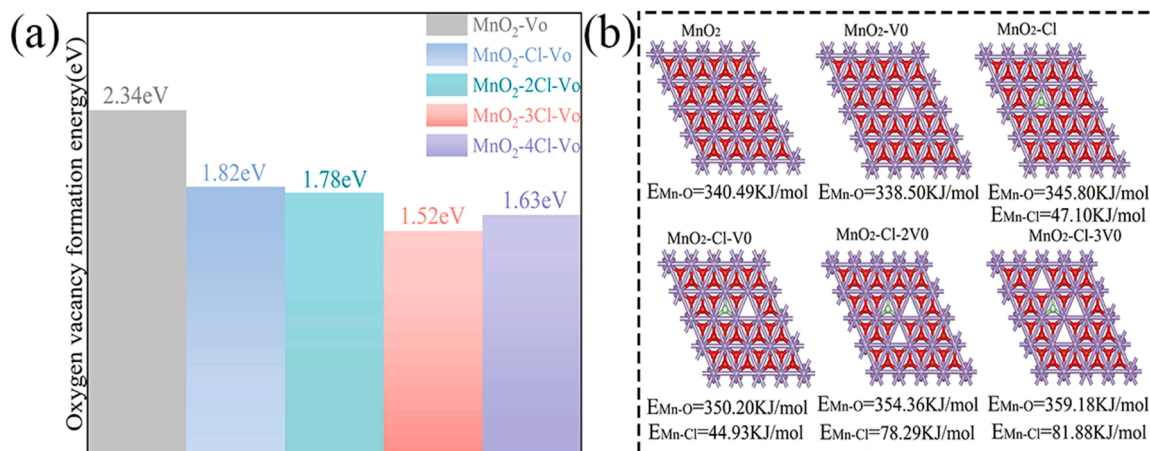
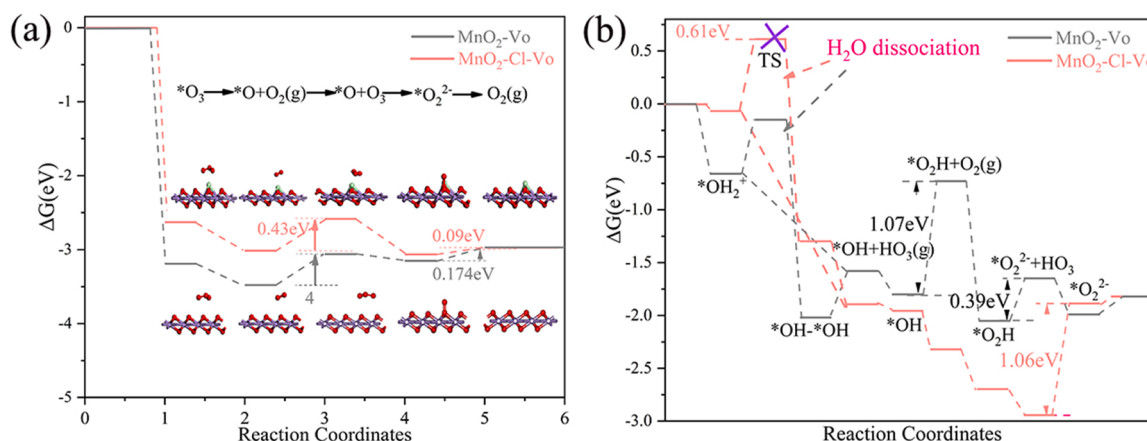


Fig. 8. (a) Effects of Cl numbers on surface oxygen vacancy formation energies on  $\text{MnO}_2$ ; (b) Effects of oxygen vacancies and chlorine-doping on the bond strength of Mn–O and Mn–Cl.



**Fig. 10.** Free energy diagrams of  $\text{O}_3$  decomposition over  $\text{MnO}_2\text{-Vo}$  and  $\text{MnO}_2\text{-Cl-Vo}$ . (a) under dry condition; (b) under humid condition (purple, red and green balls represented Mn, O, and Cl atoms, respectively).

non-dissociative adsorption of water to form adsorbed OH and  $\text{H}_2\text{O}$  coexist on  $\text{MnO}_2\text{-Vo}$ . The energy barrier for the reaction of surface OH with ozone to produce  $\text{HO}_2$  species (reaction H4) is endothermic (1.07 eV). Once surface  $\text{HO}_2$  is formed, the energy barrier from  $\text{HO}_2$  to surface adsorbed  $\text{O}_2^2-/ \text{O}_2^-$  is 0.39 eV. The final step, i.e., the desorption of dioxygen species ( $\text{O}_2^2-/ \text{O}_2^-$ ), is 0.173 eV. Apparently, by DFT calculation, the intermediates of surface OH,  $\text{HO}_2$ , and  $\text{O}_2^2-/ \text{O}_2^-$  are the main rate-limiting products, which is consistent with in-situ DRIFTS result of ozone decomposition on  $\text{MnO}_2\text{-0.5}$  under humid condition. Over the  $\text{MnO}_2\text{-Cl-Vo}$ , the  $\text{H}_2\text{O}$  adsorption (H1) can spontaneously occur ( $-0.07$  eV), while the water dissociation needs to overcome the energy barrier (0.68 eV). This implies that the dissociative adsorption of water hardly occurs on  $\text{MnO}_2\text{-Cl-Vo}$ . In addition, the following five elementary reactions over  $\text{MnO}_2\text{-Cl-Vo}$  are all exothermic, suggesting that intermediates such as OH and  $\text{HO}_2$  would not accumulate on the surface of chlorine-doped  $\delta\text{-MnO}_2$ . Only the final step, i.e., the desorption of dioxygen species ( $\text{O}_2^2-/ \text{O}_2^-$ ), is endothermic. Thus dioxygen species may accumulate on the surface. However, for the entire reaction chain, the total reaction barrier over  $\text{MnO}_2\text{-Cl-Vo}$  is 1.09 eV, while it is 1.64 eV over  $\text{MnO}_2\text{-Vo}$ . Thus, the ozone is more easily decomposed over  $\text{MnO}_2\text{-Cl-Vo}$ .

The above DFT calculation results fully indicate that the chlorine-doping in  $\delta\text{-MnO}_2$  significantly decreases the formation energy of oxygen vacancies, and the presence of a Cl atom nearby oxygen vacancy sufficiently increases its resistance to water vapor and inhibits surface hydroxylation. As a result, the chlorine-doping significantly increases the catalytic activity and stability of  $\delta\text{-MnO}_2$  for ozone decomposition under dry and humid conditions.

#### 4. Conclusion

Chlorine-doped  $\delta\text{-MnO}_2$  with a hierarchical porous structure was successfully synthesized with the one-step hydrothermal method, which exhibited excellent activity for ozone decomposition under both dry and humid conditions. The chlorine doping in  $\delta\text{-MnO}_2$  significantly increased the abundance of oxygen vacancies. In-situ DRIFTS indicated that the oxygen vacancies of chlorine-doped  $\delta\text{-MnO}_2$  were less adsorbed by water or dissociated hydroxyl species. DFT calculations demonstrated that chlorine doping not only significantly decreases the formation energy of oxygen vacancy and the reaction barriers in dry or highly moist condition, but also enhances the desorption potentials of water and reaction intermediates. Thus, the relative adsorption potentials of ozone on the oxygen vacancies are increased, and ozone decomposes more easily over chlorine-doped  $\delta\text{-MnO}_2$  in entire humidities.

#### CRediT authorship contribution statement

**Zhang Wu:** Experiment design, Methodology, Data acquisition and curation, Investigation, Writing – original manuscript, DFT calculations. **Pengyi Zhang:** Supervision, Project administration, Funding acquisition, manuscript writing and editing. All authors have read and agreed to the published version of this manuscript. **Shaopeng Rong:** DFT calculations. **Jingbo Jia:** Supervision and editing.

#### Declaration of Competing Interest

The authors declare that they have no known competing financial interests or personal relationships that could have appeared to influence the work reported in this paper.

#### Data Availability

Data will be made available on request.

#### Acknowledgements

This work was financially supported by the National Natural Science Foundation of China (22076094), Science & Technology Innovation Program of Shunde of Foshan City (2130218002526), Tsinghua-Foshan Innovation Special Fund (2021THFS0503) and special fund of State Key Joint Laboratory of Environment Simulation and Pollution Control (21K03ESPCT). The authors would like to thank Jianxia Duan and Wenqing Yao at the NCESBJ (National Center of Electron Spectroscopy in Beijing) for help with XPS measurements.

#### Appendix A. Supporting information

Supplementary data associated with this article can be found in the online version at [doi:10.1016/j.apcatb.2023.122900](https://doi.org/10.1016/j.apcatb.2023.122900).

#### References

- [1] A. Stenke, Natural control on ozone pollution, *Nat. Clim. Chang.* 10 (2020) 101–102.
- [2] O.R. Cooper, A.O. Langford, D.D. Parrish, D.W. Fahey, Challenges of a lowered U.S. ozone standard, *Science* 348 (2015) 1096–1097.
- [3] M. Li, H. Dong, B. Wang, W. Zhao, M.J. Zare Sakhvidi, L. Li, G. Lin, J. Yang, Association between ambient ozone pollution and mortality from a spectrum of causes in Guangzhou, China, *Sci. Total Environ.* 754 (2021), 142110.
- [4] S.A. Meo, F.J. Almutairi, A.A. Abukhalaf, O.M. Alessa, T. Al-Khlaiwi, A.S. Meo, Sandstorm and its effect on particulate matter PM 2.5, carbon monoxide, nitrogen dioxide, ozone pollutants and SARS-CoV-2 cases and deaths, *Sci. Total Environ.* 795 (2021), 148764.



- [5] K. Li, D.J. Jacob, H. Liao, J. Zhu, V. Shah, L. Shen, K.H. Bates, Q. Zhang, S. Zhai, A two-pollutant strategy for improving ozone and particulate air quality in China, *Nat. Geosci.* 12 (2019) 906–910.
- [6] B. Dhandapani, S.T. Oyama, Gas phase ozone decomposition catalysts, *Appl. Catal. B Environ.* 11 (1997) 129–166.
- [7] R. Radhakrishnan, S.T. Oyama, Ozone decomposition over manganese oxide supported on  $\text{ZrO}_2$  and  $\text{TiO}_2$ : a kinetic study using in situ laser raman spectroscopy, *J. Catal.* 199 (2001) 282–290.
- [8] B. Kasprzyk-Hordern, M. Ziółek, J. Nawrocki, Catalytic ozonation and methods of enhancing molecular ozone reactions in water treatment, *Appl. Catal. B Environ.* 46 (2003) 639–669.
- [9] B. Dhandapani, S.T. Oyama, Gas phase ozone decomposition catalysts, *Appl. Catal. B Environ.* 11 (1997) 129–166.
- [10] M. Namdari, C.-S. Lee, F. Haghighat, Active ozone removal technologies for a safe indoor environment: a comprehensive review, *Build. Environ.* 187 (2021), 107370.
- [11] P.M. Álvarez, J.F. García-Araya, F.J. Beltrán, I. Giraldez, J. Jaramillo, V. Gómez-Serrano, The influence of various factors on aqueous ozone decomposition by granular activated carbons and the development of a mechanistic approach, *Carbon* 44 (2006) 3102–3112.
- [12] K.-C. Cho, K.-C. Hwang, T. Sano, K. Takeuchi, S. Matsuzawa, Photocatalytic performance of Pt-loaded  $\text{TiO}_2$  in the decomposition of gaseous ozone, *J. Photochem. Photobiol. A-Chem.* 161 (2001) 155–161.
- [13] C.-L. Chang, T.-S. Lin, Pt/Rh and Pd/Rh catalysts used for ozone decomposition and simultaneous elimination of ozone and carbon monoxide, *React. Kinet. Catal. Lett.* 86 (2005) 91–98.
- [14] Z. Hao, D. Cheng, Y. Guo, Y. Liang, Supported gold catalysts used for ozone decomposition and simultaneous elimination of ozone and carbon monoxide at ambient temperature, *Appl. Catal. B Environ.* 33 (2001) 217–222.
- [15] S. Imamura, M. Ikebata, T. Ito, T. Ogita, Decomposition of ozone on a silver catalyst, *Ind. Eng. Chem. Res.* 30 (1991) 217–221.
- [16] A. Naydenov, P. Konova, P. Nikolov, F. Klingstedt, N. Kumar, D. Kovacheva, P. Stefanov, R. Stoyanova, D. Mehandjiev, Decomposition of ozone on  $\text{Ag/SiO}_2$  catalyst for abatement of waste gases emissions, *Catal. Today* 137 (2008) 471–474.
- [17] M.A. Alsheyab, A.H. Muñoz, Comparative study of ozone and  $\text{MnO}_2/\text{O}_3$  effects on the elimination of TOC and COD of raw water at the Valmayor station, *Desalination* 207 (2007) 179–183.
- [18] X. Liang, L. Wang, T. Wen, H. Liu, J. Zhang, Z. Liu, C. Zhu, C. Long, Mesoporous poorly crystalline  $\alpha\text{-Fe}_2\text{O}_3$  with abundant oxygen vacancies and acid sites for ozone decomposition, *Sci. Total Environ.* 804 (2021), 150161.
- [19] C. Dong, J. Yang, L. Xie, G. Cui, W. Fang, J. Li, Catalytic ozone decomposition and adsorptive VOCs removal in bimetallic metal-organic frameworks, *Nat. Commun.* 13 (2022) 4991.
- [20] S. Gong, X. Wu, J. Zhang, N. Han, Y. Chen, Facile solution synthesis of  $\text{Cu}_2\text{O}-\text{CuO}-\text{Cu}(\text{OH})_2$  hierarchical nanostructures for effective catalytic ozone decomposition, *Crystengcomm* 20 (2018) 3096–3104.
- [21] S. Gong, A. Wang, Y. Wang, H. Liu, N. Han, Y. Chen, Heterostructured Ni/NiO nanocatalysts for ozone decomposition, *ACS Appl. Nano Mater.* 3 (2019) 597–607.
- [22] R. Radhakrishnan, S.T. Oyama, J.G. Chen, K. Asakura, Electron transfer effects in ozone decomposition on supported manganese oxide, *J. Phys. Chem. B* 105 (2001) 4245–4253.
- [23] G. Zhu, W. Zhu, Y. Lou, J. Ma, W. Yao, R. Zong, Y. Zhu, Encapsulate  $\alpha\text{-MnO}_2$  nanofiber within graphene layer to tune surface electronic structure for efficient ozone decomposition, *Nat. Commun.* 12 (2021) 4152.
- [24] Z. Xu, W. Yang, W. Si, J. Chen, Y. Peng, J. Li, A novel gamma-like  $\text{MnO}_2$  catalyst for ozone decomposition in high humidity conditions, *J. Hazard. Mater.* 420 (2021), 126641.
- [25] C. Fang, C. Hu, D. Li, J. Chen, M. Luo, Unravelling the efficient catalytic performance of ozone decomposition over nitrogen-doped manganese oxide catalysts under high humidity, *N. J. Chem.* 44 (2020) 17993–17999.
- [26] R. Cao, L. Li, P. Zhang, Macroporous  $\text{MnO}_2$ -based aerogel crosslinked with cellulose nanofibers for efficient ozone removal under humid condition, *J. Hazard. Mater.* 407 (2021), 124793.
- [27] R. Cao, L. Li, P. Zhang, L. Gao, S. Rong, Regulating oxygen vacancy in ultrathin  $\delta\text{-MnO}_2$  nanosheets with superior activity for gaseous ozone decomposition, *Environ. Sci.: Nano* 8 (2021) 1628–1641.
- [28] M.P. Esfahani, C. Wu, A.D. Visscher, Theoretical estimation of the apparent rate constants for ozone decomposition in gas and aqueous phases using ab initio calculations, *Can. J. Chem. Eng.* 98 (2019) 274–280.
- [29] T. Gopi, G. Swetha, S. Chandra Shekar, C. Ramakrishna, B. Saini, R. Krishna, P.V. L. Rao, Catalytic decomposition of ozone on nanostructured potassium and proton containing  $\delta\text{-MnO}_2$  catalysts, *Catal. Commun.* 92 (2017) 51–55.
- [30] N. Brodu, M.H. Manero, C. Andriantsiferana, J.S. Pic, H. Valdés, Role of Lewis acid sites of ZSM-5 zeolite on gaseous ozone abatement, *Chem. Eng. J.* 231 (2013) 281–286.
- [31] W. Hong, T. Zhu, Y. Sun, H. Wang, X. Li, F. Shen, Enhancing oxygen vacancies by introducing  $\text{Na}^+$  into OMS-2 tunnels to promote catalytic ozone decomposition, *Environ. Sci. Technol.* 53 (2019) 13332–13343.
- [32] Y. Yu, H. Wang, H. Li, P. Tao, T. Sun, Influence of water molecule on active sites of manganese oxide-based catalysts for ozone decomposition, *Chemosphere* 298 (2022), 134187.
- [33] W. Li, G.V. Gibbs, S. Ted, Oyama, mechanism of ozone decomposition on a manganese oxide catalyst.1. In situ Raman spectroscopy and ab initio molecular orbital calculations, *J. Am. Chem. Soc.* 35 (1998) 9041–9046.
- [34] S. Gong, Z. Xie, W. Li, X. Wu, N. Han, Y. Chen, Highly active and humidity resistive perovskite  $\text{LaFeO}_3$  based catalysts for efficient ozone decomposition, *Appl. Catal. B Environ.* 241 (2019) 578–587.
- [35] W. Hong, M. Shao, T. Zhu, H. Wang, Y. Sun, F. Shen, X. Li, To promote ozone catalytic decomposition by fabricating manganese vacancies in  $\epsilon\text{-MnO}_2$  catalyst via selective dissolution of Mn-Li precursors, *Appl. Catal. B Environ.* 274 (2020), 119088.
- [36] W. Hong, J. Ma, T. Zhu, H. He, H. Wang, Y. Sun, F. Shen, X. Li, To enhance water resistance for catalytic ozone decomposition by fabricating  $\text{H}_2\text{O}$  adsorption-site in OMS-2 tunnels, *Appl. Catal. B Environ.* 297 (2021), 120466.
- [37] W.T. Tsai, C.Y. Chang, F.H. Jung, C.Y. Chiu, W.H. Huang, Y.H. Yu, H.T. Liou, Y. Ku, J.N. Chen, C.F. Mao, Catalytic decomposition of ozone in the presence of water vapor, *J. Environ. Sci. Health Part A-Toxic./Hazard. Subst. Environ. Eng.* 33 (1998) 1705–1717.
- [38] J.M. Roscoe, J.P.D. Abbatt, Diffuse reflectance FTIR study of the interaction of alumina surfaces with ozone and water vapor, *J. Phys. Chem. A* 109 (2005) 9028–9034.
- [39] H. Valdés, F.J. Ulloa, V.A. Solar, M.S. Cepeda, F. Azzolina-Jury, F. Thibault-Starzyk, New insight of the influence of acidic surface sites of zeolite on the ability to remove gaseous ozone using operando DRIFTS studies, *Microporous Mesoporous Mat.* 294 (2020), 109912.
- [40] Y. Liu, W. Zong, H. Zhou, D. Wang, R. Cao, J. Zhan, L. Liu, B.W.L. Jang, Tuning the interlayer cations of birnessite-type  $\text{MnO}_2$  to enhance its oxidation ability for gaseous benzene with water resistance, *Catal. Sci. Technol.* 8 (2018) 5344–5358.
- [41] G. Zhu, J. Zhu, W. Li, W. Yao, R. Zong, Y. Zhu, Q. Zhang, Tuning the  $\text{K}^+$  concentration in the tunnels of  $\alpha\text{-MnO}_2$  to increase the content of oxygen vacancy for ozone elimination, *Environ. Sci. Technol.* 52 (2018) 8684–8692.
- [42] L. Li, P. Zhang, R. Cao, Porous manganese oxides synthesized with natural products at room temperature: a superior humidity-tolerant catalyst for ozone decomposition, *Catal. Sci. Technol.* 10 (2020) 2254–2267.
- [43] J. Zhou, L. Qin, W. Xiao, C. Zeng, N. Li, T. Lv, H. Zhu, Oriented growth of layered- $\text{MnO}_2$  nanosheets over  $\alpha\text{-MnO}_2$  nanotubes for enhanced room-temperature HCHO oxidation, *Appl. Catal. B Environ.* 207 (2017) 233–243.
- [44] Y. Meng, W. Song, H. Huang, Z. Ren, S.Y. Chen, S.L. Suib, Structure-property relationship of bifunctional  $\text{MnO}_2$  nanostructures: highly efficient, ultra-stable electrochemical water oxidation and oxygen reduction reaction catalysts identified in alkaline media, *J. Am. Chem. Soc.* 136 (2014) 11452–11464.
- [45] Y. Kou, J. Liu, Y. Li, S. Qu, C. Ma, Z. Song, X. Han, Y. Deng, W. Hu, C. Zhong, Electrochemical oxidation of chlorine-doped  $\text{Co}(\text{OH})_2$  nanosheet arrays on carbon cloth as a bifunctional oxygen electrode, *ACS Appl. Mater. Interfaces* 10 (2018) 796–805.
- [46] C. Liu, Y. Zhang, F. Dong, A.H. Reshak, L. Ye, N. Pinna, C. Zeng, T. Zhang, H. Huang, Chlorine intercalation in graphitic carbon nitride for efficient photocatalysis, *Appl. Catal. B Environ.* 203 (2017) 465–474.
- [47] Y. Liu, P. Zhang, Catalytic decomposition of gaseous ozone over todorokite-type manganese dioxides at room temperature: effects of cerium modification, *Appl. Catal. A Gen.* 530 (2017) 102–110.
- [48] Y. Yang, J. Jia, Y. Liu, P. Zhang, The effect of tungsten doping on the catalytic activity of  $\alpha\text{-MnO}_2$  nanomaterial for ozone decomposition under humid condition, *Appl. Catal. A Gen.* 562 (2018) 132–141.
- [49] G. Chen, Y. Cai, H. Zhang, D. Hong, S. Shao, C. Tu, Y. Chen, F. Wang, B. Chen, Y. Bai, X. Wang, Q. Dai, Pt and Mo Co-decorated  $\text{MnO}_2$  nanorods with superior resistance to  $\text{H}_2\text{O}$ , sintering, and HCl for catalytic oxidation of chlorobenzene, *Environ. Sci. Technol.* 55 (2021) 14204–14214.
- [50] G. Li, N. Li, Y. Sun, Y. Qu, Z. Jiang, Z. Zhao, Z. Zhang, J. Cheng, Z. Hao, Efficient defect engineering in Co-Mn binary oxides for low-temperature propane oxidation, *Appl. Catal. B Environ.* 282 (2021), 119512.
- [51] S. Rong, K. Li, P. Zhang, F. Liu, J. Zhang, Potassium associated manganese vacancy in birnessite-type manganese dioxide for airborne formaldehyde oxidation, *Catal. Sci. Technol.* 8 (2018) 1799–1812.
- [52] W. Zhao, M. Bajdich, S. Carey, A. Vojvodic, J.K. Nørskov, C.T. Campbell, Water dissociative adsorption on  $\text{NiO}(111)$ : energetics and structure of the hydroxylated surface, *ACS Catal.* 6 (2016) 7377–7384.
- [53] R. Mu, Z.J. Zhao, Z. Dohnalek, J. Gong, Structural motifs of water on metal oxide surfaces, *Chem. Soc. Rev.* 46 (2017) 1785–1806.
- [54] J. Wang, Y. Dang, A.G. Meguerdichian, S. Dissanayake, T. Kankanam-Kapuge, S. Bamonte, Z.M. Tobin, L.A. Achola, S.L. Suib, Water harvesting from the atmosphere in arid areas with manganese dioxide, *Environ. Sci. Technol. Lett.* 7 (2019) 48–53.
- [55] S. Parveen, Kavyashree, S.N. Pandey, Electrochemical study of 3D hierarchical dandelion-fiber flake-like structure of  $\text{Al}(\text{OH})_3/\text{MnO}_2$  nanocomposite thin film for future supercapacitor applications, *Electrochim. Acta* 319 (2019) 832–842.
- [56] G. Li, M. Jiang, Q. Liao, R. Ding, Y. Gao, L. Jiang, D. Zhang, S. Chen, H. He, Directly anchoring Ag single atoms on  $\alpha\text{-MnO}_2$  nanorods as efficient oxygen reduction catalysts for Mg-air fuel cell, *J. Alloy. Compd.* 858 (2021), 157672.
- [57] H. Deng, S. Kang, J. Ma, L. Wang, C. Zhang, H. He, Role of structural defects in  $\text{MnO}_2$  promoted by Ag doping in the catalytic combustion of volatile organic compounds and ambient decomposition of  $\text{O}_3$ , *Environ. Sci. Technol.* 53 (2019) 10871–10879.
- [58] H. Deng, H. Yi, X. Tang, Q. Yu, P. Ning, L. Yang, Adsorption equilibrium for sulfur dioxide, nitric oxide, carbon dioxide, nitrogen on 13X and 5A zeolites, *Chem. Eng. J.* 188 (2012) 77–85.
- [59] J. Wu, T. Su, Y. Jiang, X. Xie, Z. Qin, H. Ji, In situ DRIFTS study of  $\text{O}_3$  adsorption on  $\text{CaO}$ ,  $\gamma\text{-Al}_2\text{O}_3$ ,  $\text{CuO}$ ,  $\alpha\text{-Fe}_2\text{O}_3$  and  $\text{ZnO}$  at room temperature for the catalytic ozonation of cinnamaldehyde, *Appl. Surf. Sci.* 412 (2017) 290–305.
- [60] J. Dong, X. Zhang, V. Briega-Martos, X. Jin, J. Yang, S. Chen, Z. Yang, D. Wu, J. M. Feliu, C.T. Williams, Z. Tian, J. Li, In situ Raman spectroscopic evidence for oxygen reduction reaction intermediates at platinum single-crystal surfaces, *Nat. Energy* 4 (2018) 60–67.

- [61] C. Li, Q. Xin, X. Guo, Surface oxygen species and their reactivities in the mild oxidation of ethylene on cerium oxide studied by FT-IR spectroscopy, *Catal. Lett.* 12 (1992) 297–306.
- [62] M. Nakamura, S.-i Fujita, N. Takezawa, The state of adsorbed oxygen species formed in the decomposition of  $N_2O$  on  $CaO$ , *Catal. Lett.* 14 (1992) 315–320.
- [63] C. Li, K. Domen, K.-I. Maruya, T. Onishi, Oxygen exchange reactions over cerium oxide An FT-IR study, *J. Catal.* 123 (1990) 436–442.
- [64] J.M. Roscoe, J.P.D. Abbatt, Diffuse reflectance FTIR study of the interaction of alumina surfaces with ozone and water vapor, *J. Phys. Chem. A* 40 (2005) 9028–9034.
- [65] J. Jia, P. Zhang, L. Chen, Catalytic decomposition of gaseous ozone over manganese dioxides with different crystal structures, *Appl. Catal. B Environ.* 189 (2016) 210–218.
- [66] Z. Sun, Y. Si, S. Zhao, Q. Wang, S. Zang, Ozone decomposition by a manganese-organic framework over the entire humidity range, *J. Am. Chem. Soc.* 143 (2021) 5150–5157.
- [67] S. Afzal, X. Quan, J. Zhang, High surface area mesoporous nanocast  $LaMO_3$  ( $M = Mn, Fe$ ) perovskites for efficient catalytic ozonation and an insight into probable catalytic mechanism, *Appl. Catal. B Environ.* 206 (2017) 692–703.